

Demonstration of a geostatistical approach to physically consistent downscaling of climate modeling simulations

Sanjeev Kumar Jha,¹ Gregoire Mariethoz,¹ Jason P. Evans,² and Matthew F. McCabe^{1,3}

Received 30 June 2012; revised 21 September 2012; accepted 15 November 2012; published XX Month 2013.

[1] A downscaling approach based on multiple-point geostatistics (MPS) is presented. The key concept underlying MPS is to sample spatial patterns from within training images, which can then be used in characterizing the relationship between different variables across multiple scales. The approach is used here to downscale climate variables including skin surface temperature (TSK), soil moisture (SMOIS), and latent heat flux (LH). The performance of the approach is assessed by applying it to data derived from a regional climate model of the Murray-Darling basin in southeast Australia, using model outputs at two spatial resolutions of 50 and 10 km. The data used in this study cover the period from 1985 to 2006, with 1985 to 2005 used for generating the training images that define the relationships of the variables across the different spatial scales. Subsequently, the spatial distributions for the variables in 2006 are determined at 10 km resolution using the 50 km resolution data as input. The MPS geostatistical downscaling approach reproduces the spatial distribution of TSK, SMOIS, and LH at 10 km resolution with the correct spatial patterns over different seasons, while providing uncertainty estimates through the use of multiple realizations. The technique has the potential to not only bridge issues of spatial resolution in regional and global climate model simulations but also in feature sharpening in remote sensing applications through image fusion, filling gaps in spatial data, evaluating downscaled variables with available remote sensing images, and aggregating/disaggregating hydrological and groundwater variables for catchment studies.

Citation: Jha, S. K., G. Mariethoz, J. P. Evans, and M. F. McCabe (2013), Demonstration of a geostatistical approach to physically consistent downscaling of climate modeling simulations, *Water Resour. Res.*, 49, doi:10.1029/2012WR012602.

1. Introduction

[2] Characterizing changes in local climate variables is required to better understand the movement of water through the atmosphere, land surface, and subsurface interfaces at basin scales and to quantify the influence of potential changes in the hydrological system across a range of resolutions. Among other variables, the surface skin temperature (TSK), soil moisture (SMOIS), latent heat flux (LH), and vegetation fraction (VEGFRA) are key variables in coupling atmospheric forecasting models with land surface models [Evans *et al.*, 2011; McCumber and Pielke, 1981; Walker and Rowntree, 1977]. These variables are inherently interrelated and combine to affect water balances across catchment scales [McCabe *et al.*, 2008a]. For instance, while the amount of vegetation fraction directly influence

the SMOIS, LH, and TSK, it is likewise affected by variations in each of these other related variables through complex nonlinear relationships [Rodriguez-Iturbe, 2000].

[3] General circulation models (GCMs) provide a mechanism through which to predict the climate under scenarios of future change. However, the output of these GCMs is often too coarse (grid cells of hundreds of kilometers) for studying the potential effects of hydrological variability and change at the regional and local scale. For example, hydrological studies related to the effect of climate change on areas such as flood prediction, groundwater recharge, agricultural water use, and urban water supply all require information at the catchment scale, which is beyond the capacity of current generation GCMs to provide. To bridge the mismatch of spatial scale between the GCM and the scale of operational interest, some form of data downscaling is necessary.

[4] There are two broad categories of downscaling approaches existing in the current literature: statistical downscaling and dynamical downscaling. Comprehensive reviews on these approaches have been provided by various researchers [Evans *et al.*, 2012; Maraun *et al.*, 2010; Wilby and Wigley, 1997; Wilby, 2002], so only a summary is provided here. Statistical downscaling approaches are based mainly on regression relationships between the coarse scale information obtained from GCM (predictors) and observed variables at the local or fine scale (predictands) [Hewitson and Crane, 1996]. Statistical downscaling approaches have their own limitations, such as (i) the selection of informative predictors

¹Water Research Centre, School of Civil and Environmental Engineering, University of New South Wales, Sydney, Australia.

²Climate Change Research Center, University of New South Wales, Sydney, Australia.

³Water Desalination and Reuse Center, King Abdullah University of Science and Technology, Thuwal, Saudi Arabia.

Corresponding author: S. K. Jha, Water Research Centre, School of Civil and Environmental Engineering, University of New South Wales, Sydney, NSW 2052, Australia. (s.jha@unsw.edu.au)

is an onerous task and (ii) the predictors depend on their availability from GCM outputs and also on the region and the season under consideration. The latter limitation is crucial as it determines the characteristics of the downscaled climate scenario. In addition, the derived relationship between the predictors and predictands is assumed to be valid in a future perturbed condition, which cannot be verified [Chu *et al.*, 2010].

[5] There is no universally accepted statistical downscaling approach applicable in climate change impact studies. Therefore, a recent trend in the scientific community has been to first apply several different downscaling methods and compare the results using verification data [Raje and Mujumdar, 2011]. The output of the “best” downscaled model is then forced into the hydrological model to assess the future scenario of climate change [Liu *et al.*, 2011]. Furthermore, all relevant uncertainties stemming from the selection of the downscaling methods and hydrological methods have to be taken into account. Many researchers identify the method of statistical downscaling as a major source of uncertainty in impact studies [Segui *et al.*, 2010; Stoll *et al.*, 2011; Teutschbein *et al.*, 2011]. Further investigation of statistical downscaling approaches is therefore warranted.

[6] Statistical downscaling approaches are often preferred as they are computationally less burdensome than the other major approach: dynamic downscaling [Kidson and Thompson, 1998]. In dynamical downscaling, a regional climate model (RCM) is applied using GCM outputs as boundary conditions. This approach takes into account detailed terrain and land cover information and provides physically consistent results [Kunstmann *et al.*, 2004]. Dynamic downscaling also inherently accounts for the multivariate spatial dependencies and the cross-dependencies between variables, which statistical approaches often do not [Sain *et al.*, 2011]. Although RCMs are useful for investigating the large-scale circulation, there are limitations to their application in impact studies at the regional and local levels [Giorgi, 2006], mostly related to the need to explicitly account for model biases and the difficulty to characterize downscaling uncertainty. Furthermore, the physical simulation of the climatic system in RCMs is computationally very expensive. Hence, there is growing interest in the research community to develop statistical techniques to further downscale the RCM output to the point locations required for impact studies [Evans, 2012; Hoffmann *et al.*, 2011]. These methods vary considerably from simple spatial interpolation, weather generators and machine-learning techniques [Evans, 2012].

[7] Geostatistical simulation methods provide useful tools for analyzing spatially correlated variables. Whether in predicting point values from areal data for univariate problems [Kyriakidis, 2004; Kyriakidis and Yoo, 2005] or in the use of kriging and cokriging techniques to obtain fine resolution imagery from coarse scale images [Nishii *et al.*, 1996], there are many applications of such approaches in geology, earth science, and remote sensing [Atkinson *et al.*, 2008; Liu *et al.*, 2007; Mariethoz *et al.*, 2012; Pardo-Iguez *et al.*, 2006, 2010; Zhang *et al.*, 2012]. However, most of the existing approaches are based on linear geostatistics [Goovaerts, 1997]. Such methods rely on assumptions of linear correlation with covariates or assume a multi-Gaussian spatial

dependence, involving specific types of patterns [Journel and Zhang, 2006]. From the perspective of land-atmosphere interactions, it is known that the structure of land-atmosphere variables and their interrelationships can be highly nonlinear [Wallace and Hobbs, 2006]. As a result, new statistical downscaling approaches are needed that are capable of reproducing such nonlinear characteristics.

[8] Some geostatistical approaches to downscaling have been proposed that use multiple-point geostatistics (MPS) [Strebelle, 2002], a nonparametric approach that is free from simplifying assumptions such as linearity, maximum entropy, and multi-Gaussianity [Gómez-Hernández and Wen, 1998]. However, applications to downscaling are so far limited to cases with a single variable and, in addition, are restricted to either categorical variables such as land cover category [Boucher, 2009] or to self-similar images [Mariethoz *et al.*, 2011]. In this paper, the geostatistical approach of direct sampling (DS), based on MPS, is applied for downscaling variables typically of interest in land-atmospheric studies of the hydrological sciences. Traditional geostatistical approaches use variograms, whereas the multiple-point statistics-based approaches use training images to describe spatial continuity. The DS algorithm, as described in Mariethoz *et al.* [2010], extends the idea of MPS to continuous and multivariate problems.

[9] The MPS approach involves deriving spatial arrangements of values from a training image and storing them in a database [Strebelle, 2002]. The database is used for retrieving the conditional probabilities for the simulation. In contrast, the DS approach does not require a database and can generate stochastic fields representing complex statistical and spatial properties directly from the training image. The method can use multivariate training images, generating random fields where the (possibly nonlinear) relationships between variables are reproduced as in the training image. Such an approach is used in this study, with a training image generated from 20 years of seasonal data.

[10] The rationale of our approach is to identify the dependence between coarse- and fine-scale patterns using past observations expressed as training images. Patterns contained in these training images are resampled conditionally to local coarse values, resulting in locally accurate downscaled estimates mimicking the interscale relationships as observed in training images, i.e., past observations, where the variables are informed at all scales are considered. We demonstrate the use of the DS approach with RCM simulation data at different resolutions and by comparing the downscaled results with high-resolution RCM outputs. Unlike typical statistical downscaling approaches, the proposed method provides physically consistent spatial patterns of TSK, SMOIS, and LH over different seasons, which are then used as downscaling predictive models.

2. Methodology

2.1. Direct Sampling

[11] The methodology adopted for downscaling the climate variables is based on the DS approach. The principle of DS is to sequentially determine the value of each pixel, conditional to the values of other neighboring pixels, which can be at the same scale or at a different scale. A value is obtained by conditional sampling of the training image,

which is deemed representative of the patterns at all scales considered. This is accomplished with the following algorithm: let \mathbf{x} be a pixel in the image where the variable of interest $Z(\mathbf{x})$ needs to be downscaled. Equivalently, pixels in the training image are denoted \mathbf{y} . We denote \mathbf{N}_x as the ensemble of the n closest pixels of \mathbf{x} . Note that \mathbf{x} is a two-dimensional (2-D) vector, each of its components representing a coordinate in a 2-D Cartesian space. In the case of one variable, a neighborhood is defined around the node to be simulated as $\mathbf{N}_x = [Z(\mathbf{x} + \mathbf{h}_1), \dots, Z(\mathbf{x} + \mathbf{h}_n)]$, where $\mathbf{h}_1, \dots, \mathbf{h}_n$ represent the vectors between the pixel \mathbf{x} and the neighboring pixels. The basic idea is to find another location \mathbf{y} in the training image that has a neighborhood \mathbf{N}_y similar to \mathbf{N}_x . The training image is sampled by randomly selecting pixels contained within it and defining a neighborhood $\mathbf{N}_y = [Z(\mathbf{y} + \mathbf{h}_1), \dots, Z(\mathbf{y} + \mathbf{h}_n)]$ that has the same lag vectors as in \mathbf{N}_x . The distance $d[\mathbf{N}_x, \mathbf{N}_y]$ represents the mismatch between \mathbf{N}_x and \mathbf{N}_y . At the first occurrence of a mismatch below a given threshold t , the data at the node \mathbf{y} of the training image $Z(\mathbf{y})$ is specified at location \mathbf{x} of the simulation grid. Since the distance is under the threshold, the value at location \mathbf{y} is a sample of Z conditional to the neighborhood \mathbf{N}_x . The important feature of the DS method is that using the first sample with a distance lower than t is equivalent to sampling from the high-dimensional distribution:

$$F(Z, \mathbf{x}, \mathbf{N}_x) = \text{Prob}[Z(\mathbf{x}) \leq z | \mathbf{N}_x]. \quad (1)$$

[12] This sampling strategy was first used by *Shannon* [1948] and applied to geostatistical simulations by *Mariethoz et al.* [2010].

[13] Let us now consider a multivariate case consisting of m variables $Z_1(\mathbf{x}), \dots, Z_m(\mathbf{x})$. The joint distance between multiple variables is defined, with the objective to find pixel values matching the neighborhoods of all variables taken together. The consequence is that the values sampled from (1) will have the same cross-dependencies as observed in the multiple variables of the training image. For each variable k , $k = 1, \dots, m$, the number n_k of neighboring nodes can be the same or different. Therefore, we can define an individual neighborhood for each variable k as $\mathbf{N}_x^k = [Z_k(\mathbf{x} + \mathbf{h}_1^k), \dots, Z_k(\mathbf{x} + \mathbf{h}_{n_k}^k)]$. Then, the multivariate neighborhood consists of the ensemble of all these individual neighbors joined across all m variables: $\mathbf{N}_x = [\mathbf{N}_x^1, \dots, \mathbf{N}_x^m]$.

[14] The joint distance between multivariate neighborhoods is then a linear combination of individual distances:

$$d[\mathbf{N}_x, \mathbf{N}_y] = \sum_{k=1}^m w_k d[\mathbf{N}_x^k, \mathbf{N}_y^k], \quad (2)$$

where the weights w_k sum to 1 and represent the relative importance given to each variable. The distance function $d(\cdot)$ can be defined as any valid distance function between the vectors of values in \mathbf{N}_x and \mathbf{N}_y . A detailed description of the calculation of different types of distances is provided in *Mariethoz et al.* [2010]. Some examples of distances are Euclidean, Manhattan, or transform-invariant [*Mariethoz and Kelly*, 2011]. The Manhattan distance was used for all cases presented in this paper. Apart from the computation of the distance, the rest of the algorithm is identical to the

univariate case. It should be noted that since our approach is nonparametric, no normalization or variable transformation is necessary. The downscaling methodology is represented in Figure 1 and further described in section 3.1 to explain the process of generation of training images and conditioning data.

2.2. Dimensionality of Multivariate Training Images

[15] In much of the literature devoted to MPS, training images are “images” in the commonly accepted sense and can be either 2-D or three-dimensional (3-D), depending on the application [*Strebel*, 2002]. For example, applications to remote sensing would call for 2-D images, while applications to aquifer modeling might call for 3-D models. Space-time applications such as rainfall modeling are also 3-D because they include two dimensions in space and an additional temporal dimension. The DS approach, by introducing the possibility to use multivariate training images, extends the complexity and the dimensionality of the training image objects. The addition of several variables can be seen as a four-dimensional (4-D) construct, with coordinate k defining which variable is considered.

[16] The downscaling application implemented in this paper considers 2-D land-atmosphere variables and their temporal variations, therefore making the problem effectively 3-D. The addition of several variables considered together adds one dimension, calling for 4-D training images. Since the training images need to contain the relationship between coarse and fine scale, each variable considered needs to be present in the training image at both resolutions, therefore doubling the total number of variables.

3. Data Set and Description of Variables

[17] The focus area for the study is the Murray-Darling basin (MDB) in southeast Australia (Figure 2). With a size of approximately $1 \times 10^6 \text{ km}^2$ and supporting a population over 3×10^6 people, the MDB is the largest and most economically productive catchment in Australia. Because of its importance in the Australian economy, the effect of climate change on the long-term productivity and sustainability of the basin is of high importance. The data set used in this study was derived from the work of *Evans and McCabe* [2010], who evaluated the Weather Research and

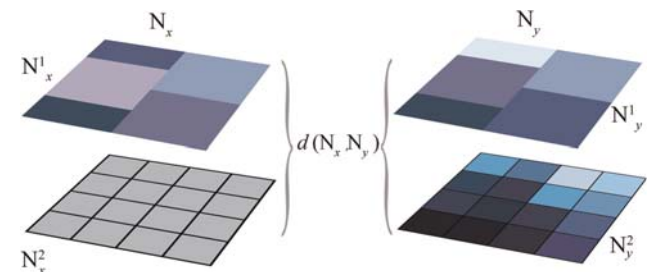


Figure 1. Description of the direct sampling approach with multivariate neighborhood and multivariate distance for two variables. (left) The available data (conditioning data) at coarse resolution and the downsampled fine grid (in gray color). (right) Training image with values of the variables known at coarse and fine resolutions.

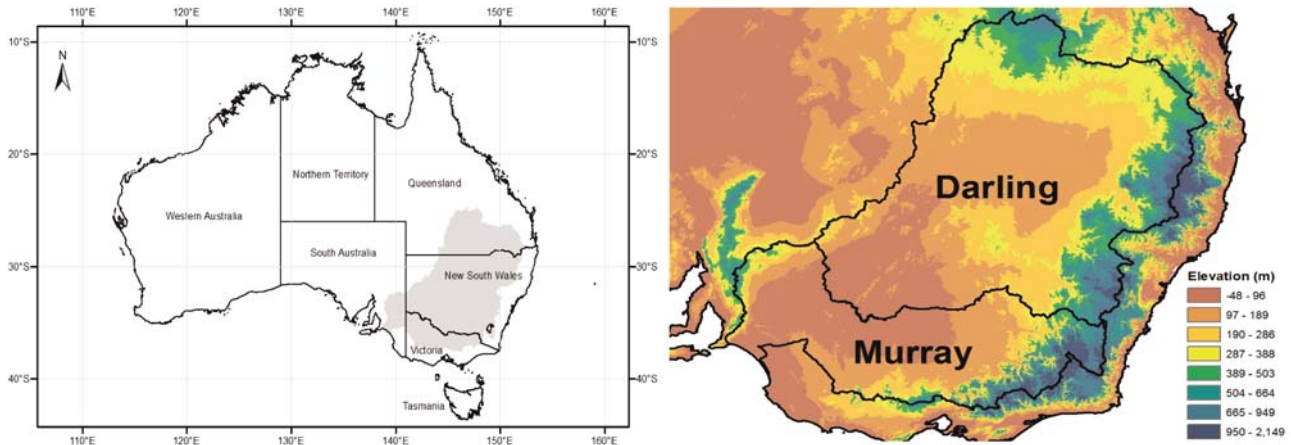


Figure 2. The Murray-Darling basin located in the southeast of Australia along with topographic profiles throughout the catchment.

Forecasting (WRF) model RCM for the period of 1985 to 2009 over the MDB, finding good agreement across multiple time scales including subdaily [Evans and Westra, 2012]. WRF has also been extensively tested over this region at the event scale using multiple physical parameterizations [Evans et al., 2012].

[18] In this study, WRF model outputs at spatial resolutions of 50 km (coarse resolution) and 10 km (fine resolution) were used to demonstrate our approach, with grids of 41×53 and 155×185 nodes, respectively. The number of cells in the simulation grid (x, y) is (161,171) with a grid cell size of 0.09° . The sample period includes daily output for the period 1985 to 2006. Twenty years of data from 1985 to 2005 at both resolutions were used as training images (calibration dataset). Using the MPS approach, downscaled 10 km predictions for each season for the year 2006 were calculated, assuming that the 50 km resolution is known for this year. The higher resolution WRF outputs for the year 2006 were used to evaluate the capability of the downscaling approach. Daily values of both the 50 and 10 km resolution of TSK, SMOIS, LH, and VEGFRA were aggregated seasonally, considering months of December, January, and February (DJF) for the summer; March, April, and May (MAM) for autumn; June, July, and August (JJA) for winter; and September, October, and November (SON) for the spring season. Note that, throughout the paper, the seasons mentioned correspond to southern hemisphere (austral) seasons.

[19] Land surface variables, such as the TSK, SMOIS, and LH, are not linearly related, with multiple thresholds in the system affecting the strength, and even the sign, of their relationships. TSK is an estimate of the temperature of a very thin surface layer of the land or water and responds rapidly to changes in direct sunshine or shade. SMOIS plays a key role in partitioning components of the water balance such as infiltration, runoff, and evaporation and can vary significantly due to large heterogeneity in land cover types, soil type, leaf area index, and topography [Brocca et al., 2012; Liu et al., 2010]. In this study, the SMOIS data correspond to the moisture content in the top 10 cm of the soil and will respond to precipitation and

evaporation much more quickly than in deeper layers [Manfreda et al., 2007; McCabe et al., 2005b]. LH describes the energy used for transporting the water from the land surface to the atmosphere as evapotranspiration, with the SMOIS condition directly influencing the evaporative flux [Kalma, 2008]. It is a critical variable in defining water and energy exchange over the Earth's terrestrial surface, with the net radiation available at the Earth surface divided principally between latent heat and sensible heat flux [Jiménez et al., 2011].

3.1. Application of DS for Downscaling

[20] The training images contain seasonal WRF outputs for 20 years, including the variables TSK, SMOIS, and LH at both fine and coarse resolutions. The statistics and patterns of land-atmosphere values for each variable are known to differ with season. As such, to represent seasonal changes in the land-atmospheric variables, a separate training image was built for each season.

[21] Each training image is a 4-D object, containing data averages for a given year and season, for 20 different years, and for the three variables to be downscaled (TSK, SMOIS, and LH) at resolutions of 50 and 10 km. As such, there are 20 training images for each season. The training images also contain the 10 km VEGFRA, latitude, and longitude as covariates in the simulation. Using equation (2), many variables can be added as covariates in the simulation. Here, latitude and longitude are considered sufficient to address the nonstationarity, but one could consider alternatives such as elevation, distance to the coast, etc. VEGFRA is included as climatological monthly values in the climate model simulations, so could also be applied to a future unknown climate state. In all, the total number of variables is nine. The reason for using all the variables simultaneously is that there exist nonlinear relationships among them, which should ideally be preserved. Due to large variations in atmospheric variables over the land and other static features such as topography, water bodies, coastal areas, etc., a constraint needs to be applied to prevent using patterns that emerge from very different locations. Including latitude and longitude in the computation of the distance has the

consequence of imposing such local consistency in the downscaled spatial features [Honarkhah and Caers, 2012], while the VEGFRA constraint limits the result to areas with similar levels of vegetation cover. The result is that patterns from similar spatial areas as their coarse counterpart are more likely to be identified and used for downscaled values. The resulting training images are assumed to contain the various higher-order statistical behavior of the system and are thereafter used as a nonparametric spatiotemporal multi-scale model.

[22] The setup of the DS model is described in Figure 1. The layers on the right-hand side represent one variable of the training image at resolutions of 50 and 10 km (i.e., the available data in the period 1985–2005). Each of the variables has the same two sets of information for each of the 20 years of data. The left-hand side indicates new data (i.e., year 2006) that needs to be downscaled. Here, the information is available only at the coarse resolution and the values of the variable at the finer grid (shown in gray color) are those to be generated. Since multivariate patterns are considered (each scale being considered as a different variable), N_x is made of both coarse (N_x^1) and fine (N_x^2) values in the simulation grid, and similarly N_y considers both scales together in the training image (N_y^1 and N_y^2). Equation (2) compares these together, therefore preserving the spatial relationships across scales. In our case, we jointly simulate three variables (LH, SMOIS, and TSK), each of which has to be considered at both fine and coarse scales.

[23] For the DS, we used neighborhoods consisting of 20 pixels for high-resolution and 20 pixels for low-resolution variables: except for the latitude and longitude for which a single neighbor (the central pixel of the pattern) is enough to define the location of a point. The distance function in (2) is used with a distance threshold of $t = 0.01$. All variables are given a weight $w_k = 0.1333$ in the distance calculation, except for latitude and longitude, which have a weight of 0.0333 to allow sampling patterns in across a reasonably broad area of the domain to be considered. Regarding parameterization of the method, we refer the reader to a comprehensive discussion and sensitivity analysis on the DS parameters provided in Meerschman *et al.* [submitted; Meerschman, 2012]. Note that the DS also allows the imposition of a temporal dependence between 1 year and the next by defining neighbors as adjacent pixels in the third dimension (corresponding to time). However, we do not impose such dependence here because, in the case of downscaling seasonal values, we assume that the temporal dependence is entirely driven by the coarse data. Our training image is a stack of 20 maps, each of which is equally likely to be considered in the conditional sampling. As the DS is a stochastic simulation method, we run the downscaling method 50 times to produce Monte-Carlo realizations, obtaining 50 different values at each point of the domain. Therefore, the results take the form of local probability distributions, which allows for an assessment of the uncertainty inherent to the downscaling procedure.

4. Results and Discussion

[24] For validation, the downscaled results are compared against the actual 10 km WRF outputs for all the variables in the year 2006. In this section, findings based on comparative

analysis of the downscaled results with this reference year are presented. The analysis is based on evaluating how well the downscaled approach reproduces the spatial features present at the fine scale. Quantitative validation of the results is examined in the subsequent section.

[25] Figure 3 presents the coarse input data and the results obtained from DS simulation runs for TSK, SMOIS, and LH for the summer of 2006, along with the reference image. The coarse data, as shown in the first row, has 50 km grids, and therefore the land features are homogenized over large areas. The color patterns in all three variables illustrate the overall distribution of the magnitude of variables, but there is no distinguishable feature available. The efficacy of DS can be seen by comparing the figures in

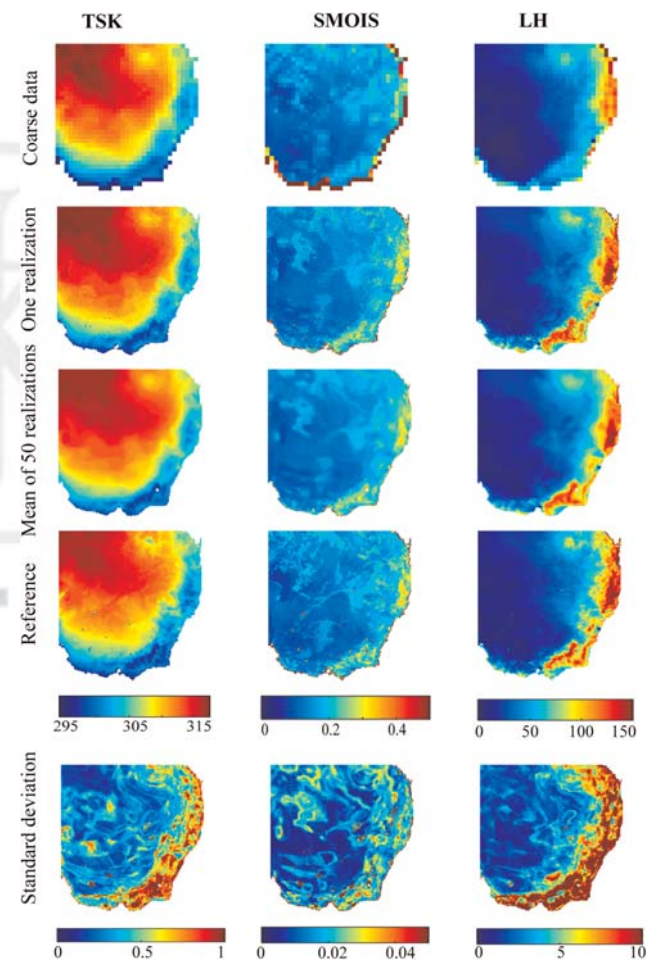


Figure 3. Establishing the efficacy of DS in downscaling TSK, SMOIS, and LH from coarse resolution to a fine grid. Summer values are displayed. Row 1: conditioning data of TSK (K), SMOIS (%), and LH (W/m^2) at 50 km resolution provided to DS. Row 2: DS output of single realization at 10 km resolution. Row 3: DS output of the mean of 50 realizations at 10 km resolution. Row 4: reference map at 10 km resolution. Row 5: standard deviation map of the variables. Note that the color bars are chosen to maximize the visibility of spatial features and do not represent the actual limits. All the figures correspond to summer 2006.

the first row with the downscaled spatial distribution of all the variables obtained from a single realization of DS in the second row. The figures in the second row not only capture the overall variation across geographical locations but also preserve detailed land features. For example, the conditioning data for LH (last figure in the first row) only show that the LH increases from west to east. There is a small area on the east coast where LH has its highest magnitude. However, the corresponding DS output (last figure in the second row), while maintaining those regions of high and low values of LH also provides insight into regions with high LH in the south of the basin, which were not visible in the conditioning data. There are also specific features on all images at the edge of the domain, related to the boundary conditions of the RCM used. Since these features are present in the training image at both scales, it is also reproduced in the downscaled realizations, as expected.

[26] The spatial distribution obtained from the mean of 50 realizations of DS is presented in the third row. The number of realization is chosen to demonstrate the performance of our approach, while balancing the inherent computational cost. By comparing figures in the second and third row, it is clear that, although the zones of high/low values of the variables remain at the same locations, by taking the mean of 50 realizations, the features have been smoothed. A single realization will preserve the textural properties of the training image but is nonunique, as it is just a single possible scenario. The DS results can be compared directly to the reference figure presented in the fourth row, which shows an excellent match for the TSK and LH and a reasonable match for the SMOIS. A quantitative assessment of this comparison is presented in section 4.2.

[27] Apart from small local scale variations, downscaled results across all realizations present similar features (refer to Figure S1 in the auxiliary material¹). The variability of the downscaled results can be seen in the standard deviation map shown in the fifth row of Figure 3. It is evident that the highest values of the standard deviation occur around the mountainous and coastal areas, where land features change abruptly to water bodies. Outside of these areas, the downscaled reproductions express similar standard deviation values with each of the three variables and exhibit little variation.

[28] Depending on the application, it may be preferable to retain either the mean or the individual realizations. If one is interested in the most probable value at each pixel (also known as conditional estimation), the mean value is appropriate. However, to correctly propagate the uncertainty in downscaling, one should keep in mind that all realizations have to be considered together. For example, if the downscaling results are used as input for a hydrological model, the hydrological model should run with each of the downscaled realizations, and the result is a set of 50 equiprobable hydrological predictions. Such predictions are generally expressed as probability density functions that could be used as input into management or policy models. Although all realizations have an equivalent chance of representing the model “reality,” for the rest of the paper,

only a single realization of the DS simulation runs are presented for analysis, due to the challenge of graphically presenting all reproductions.

4.1. Reproduction of Hydrological Variables

4.1.1. Surface Temperature (TSK)

[29] Figure 4 represents the seasonal variation of TSK obtained from DS simulation runs for summer, autumn, winter, and spring. Figures in the first column present the map of TSK at the coarse resolution of 50 km. The result of DS for a single realization is shown in the second column and the reference values in the third column. The difference plot of mean values of 50 realizations and the reference values is shown in the fourth column. Comparison of the second and third columns shows that the DS is able to capture the spatial distribution of TSK very well. In all seasons, the northern and central parts of the basin have high TSK values, while the southern region and some of the eastern coast show relatively low TSK. During the summer season, minimum and maximum values of TSK vary between 292 K and 317 K, while during the winter season they vary between 276 K and 298 K, respectively: matching the corresponding minimum and maximum values of TSK in the reference maps. Note that the color scale is different for each season in Figure 4. The corresponding standard deviation (SD) map of DS simulation runs is shown in Figure S2 (figures in the first column, auxiliary material). These figures indicate that the maximum SD, corresponding to the highest downscaling uncertainty, occurs near the southern and eastern mountainous and coastal areas, where low values of TSK occur. The difference plot shows that, during the summer season, the mean value of downscaled TSK is lower than the reference values in the northwestern region. Similar results are observed on the southern coast during the spring season. During autumn and winter, there is an improved match between the downscaled results and reference, showing zero difference. The presence of water bodies such as canals, lakes, and reservoirs produce higher values than the reference in all seasons.

4.1.2. Soil Moisture

[30] Figure 5 compares the downscaled spatial distribution of SMOIS with the reference map for different seasons. Figures in different rows are arranged in the same sequence as described previously. For all seasons, the western part of the basin has lower SMOIS relative to the reference data set. The peak SMOIS values routinely occur in the southeast. It can also be observed that SMOIS have high values during the winter season, while, in spring, SMOIS is low across the entire basin. A closer inspection of the second and third columns demonstrates that the downscaled SMOIS from the DS simulations agree reasonably well with the WRF outputs. It is clear that the SMOIS has specific features like rivers, lakes, and other water bodies that are present in the reference map but which DS has not been able to reproduce. These discrepancies are clearly visible in the difference map (figures in the fourth column), which can be attributed to the fact that there are hardly any of the land features visible in the conditioning data (figures in the first column) were provided as input to the DS. The SD maps (figures in the second column of Figure S2, auxiliary material) show that the maximum SD values occur in many areas across the entire basin but

¹Auxiliary materials are available in the HTML. doi:10.1029/2012WR012602.

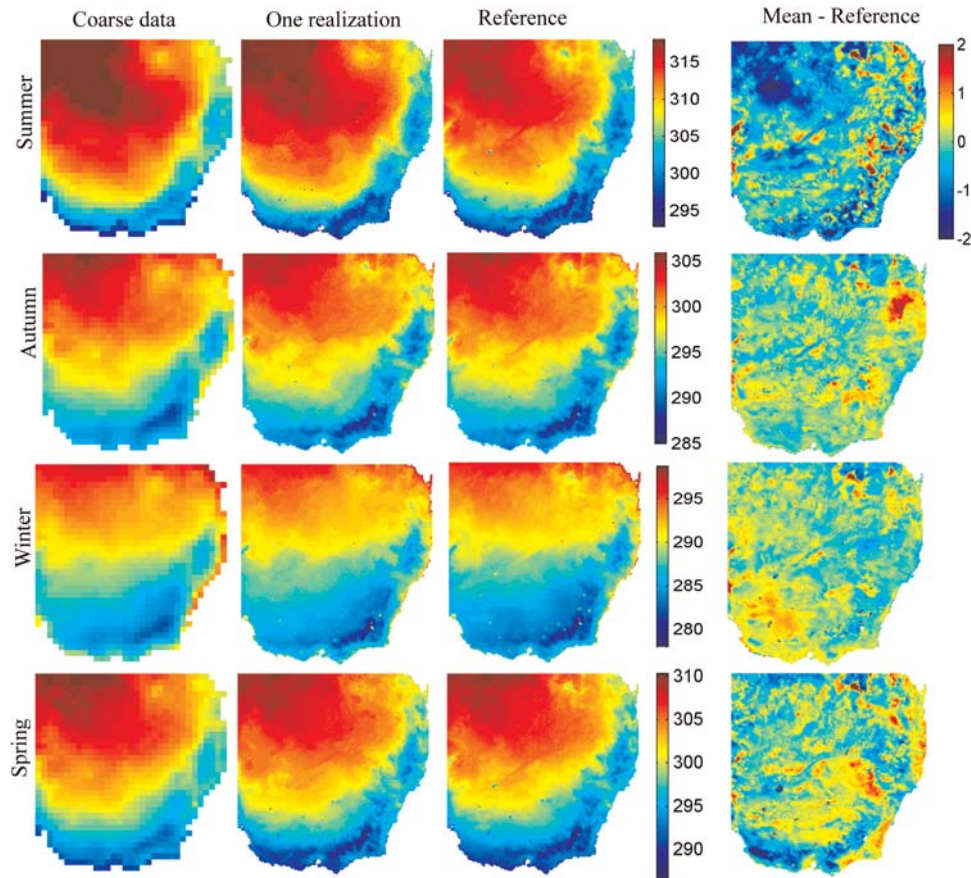


Figure 4. Summary of seasonal downscaling for the TSK. WRF output at 50 km resolution used as conditioning data in the DS approach (first column), spatial distribution of TSK (K) obtained from a single realization of DS (second column), reference values of the variables obtained from the WRF model (third column), and a plot showing difference in values between mean of 50 realizations and the reference (fourth column). The rows from the top down indicate results corresponding to results in summer, autumn, winter, and spring, respectively, for the year 2006. The color bar represents the actual limits on TSK.

predominantly in the southern part. We observed that these values are often collocated in the water bodies that are spread across the entire basin and where SMOIS is specified with a zero value.

4.1.3. Latent Heat Flux

[31] The DS heat flux results for the spatial variation of the LH are shown in Figure 6 and retaining the same layout as Figures 4 and 5. By comparing the simulation response in the second and third columns, it can be observed that the DS results are able to capture the spatial variation in LH for all of the seasons. For instance, the higher values of LH on the eastern coast are very well reproduced by DS in the summer, autumn, and spring seasons. It can also be seen that LH is high in the southeast part of the basin in the summer and spring seasons. During the winter season, very low values of LH are observed everywhere in the basin, which is again captured by the DS runs (second and third columns of row 3). Note that the color bar is different in the winter. The difference map (fourth column) shows that, throughout the basin, there is a wide range of differences between the mean values of downscaled LH from 50 realizations and the reference values. However, during the

winter season, the difference is relatively uniform over the entire basin. The SD maps (figures in the third column of Figure S2, auxiliary material) show SD patterns that are similar in all seasons except winter, when the entire basin has small and almost constant SD.

[32] The areas in the difference map where the highest errors are observed correspond to locations where the coarse variable patterns are not informative enough to characterize the smaller scale processes. For example, in Figure 4, the lower part of the domain presents high LH values for spring and summer on the fine-scale model, whereas the corresponding coarse scale is mostly featureless. The coarse scale is therefore poorly informative, and the information necessary for downscaling is simply not sufficient to identify the high LH values. This results in the observed high estimation bias (high difference map) and is confirmed by the high values also present for the same locations in the standard deviation maps.

4.2. Quantitative Measures of Error

[33] As mentioned earlier, although the simulation was run for 50 realizations to demonstrate the efficacy of DS,

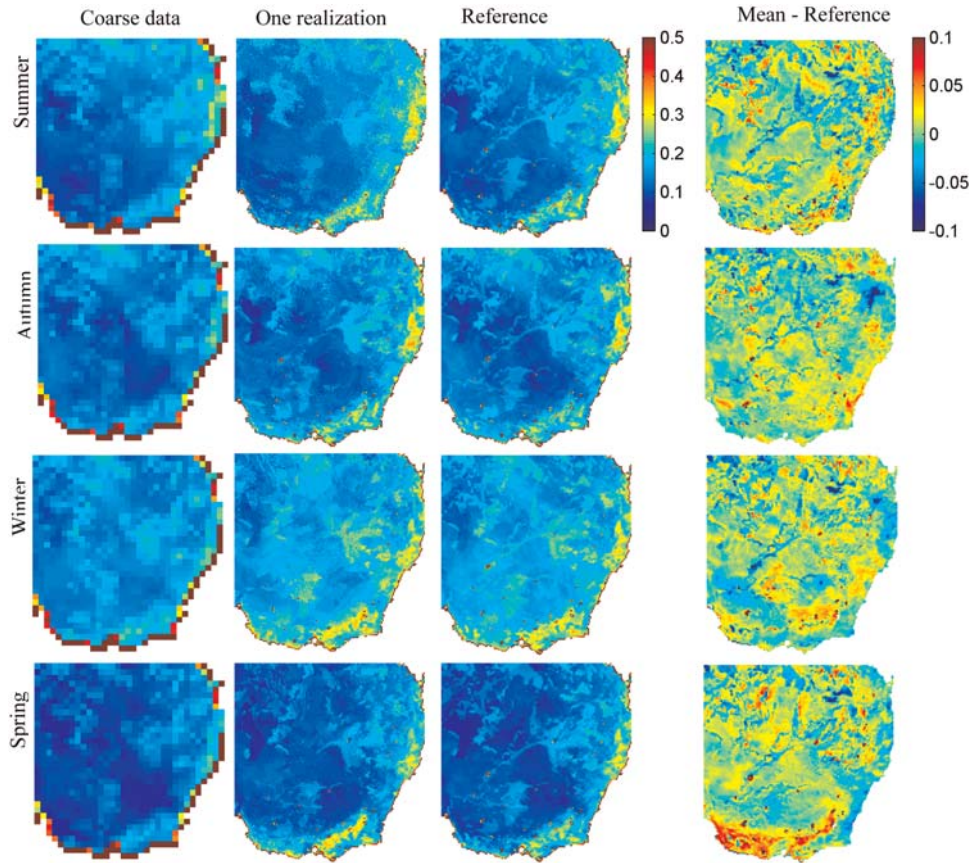


Figure 5. Summary of seasonal downscaling for the SMOIS. WRF output at 50 km resolution used as conditioning data in the DS approach (first column); spatial distribution of SMOIS (%) obtained from a single realization of DS (second column); reference values of the variables obtained from the WRF model (third column); and a plot showing difference in values between mean of 50 realizations and the reference (fourth column). The rows from the top down indicate results corresponding to results in summer, autumn, winter, and spring, respectively, for the year 2006. Note that the color bar is chosen to vary between 0 and 0.5 to enhance the visualization. The actual SMOIS varies between 0 and 1.

only results from a single realization were presented. In addition, all the downscaled values from 50 realizations were plotted against the single reference values for summer and winter in the scatter plots presented in Figures 7 and 8, respectively. The average values of the root-mean-square error (RMSE), bias, correlation coefficient (R^2), and SD of downscaled values from all 50 realizations are presented in the figures. From the first row of Figure 7, it is clear that in the case of TSK and LH, all points lay around the reference line of slope 1 and intercept 0. However, there are a significant number of points spread away from the reference line for the SMOIS plot. The scatter plots show that the downscaled values are well correlated with the reference WRF datasets, with a small number of outliers. From Figures 7 and 8, it can also be observed that for TSK and SMOIS, the scatter remains quite consistent across the different seasons. However, the scatter plot for LH changes over the seasons. In summer, the plot shows wide scatter, indicating too much spatial variation in the values of LH, which is also visible in Figure 6. The results for spring and autumn show similarly shaped distributions but different values

(see Figures S3 and S4, auxiliary material). The scatter in LH is very low during the autumn and winter seasons. A wide scatter was observed in LH during spring, which can also be verified from Figure 6. The RMSE of TSK and SMOIS are almost the same in all seasons. For the LH, we observe variations in the RMSE and also in the biases over different seasons. These can be attributed to the fact that latitude and longitude may not be entirely sufficient to represent the nonstationarity, resulting in inadequate application of the method for certain locations. Additional information such as distance to the sea might capture the nonstationarity better. Another consideration is that the parameters of the DS have been adjusted for all seasons together. To address this, one could undertake a sensitivity analysis to establish the best weights and the distance threshold parameters to use for each season: an issue that requires further investigation and is the topic of current work.

[34] The histograms of errors are presented in the lower part of Figure 7, which are estimated by subtracting the reference values from the mean of 50 realizations. The errors are centered around 0 and mostly unbiased. For TSK, the

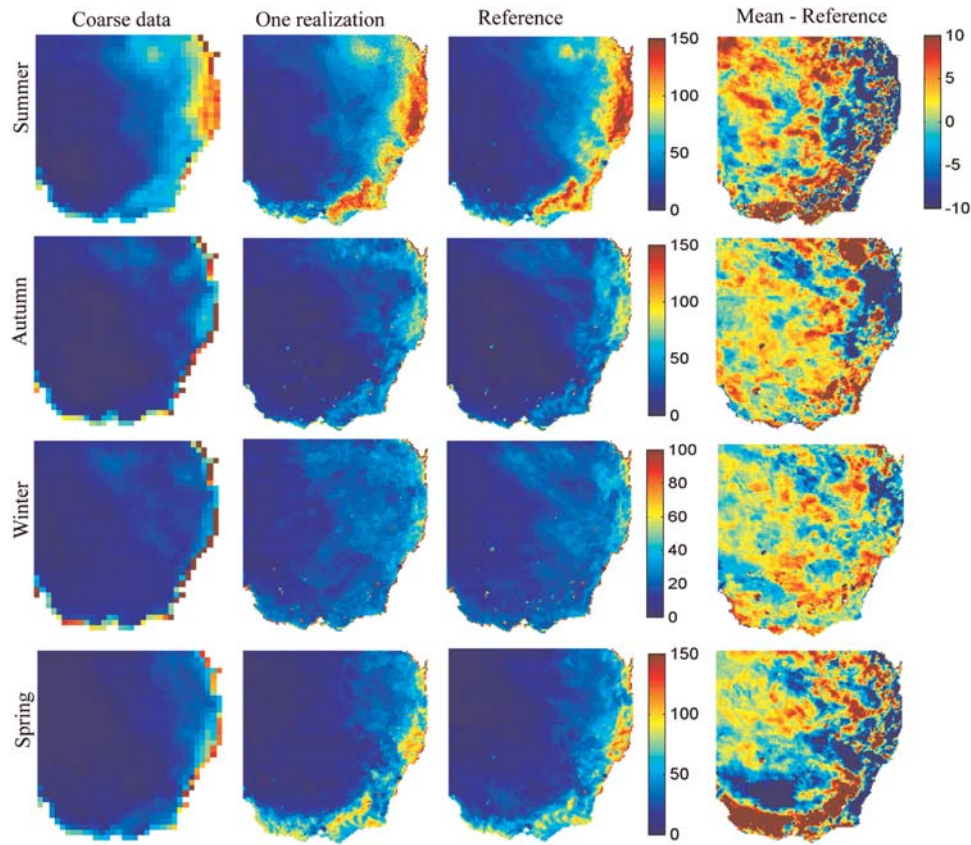


Figure 6. Summary of seasonal downscaling for the LH. WRF output at 50 km resolution used as conditioning data in the DS approach (first column); spatial distribution of LH (W/m^2) obtained from a single realization of DS (second column); reference values of the variables obtained from the WRF model (third column); and a plot showing difference in values between mean of 50 realizations and the reference (fourth column). The rows from the top down indicate results corresponding to results in summer, autumn, winter, and spring, respectively, for the year 2006. The color bar represents the actual limits on LH.

errors can reach up to 5 K, whereas the errors for SMOIS vary between 0% and 2%. The errors in LH are of higher magnitude, reaching up to 50 W/m^2 . These errors fall within the expected range previously reported in terms of RMSE as 1–8 K for TSK [Ferguson and Wood, 2010; McCabe et al., 2008b; Wan et al., 2002], 3%–7% for SMOIS [Drusch et al., 2004; Liu et al., 2011; McCabe et al., 2005a] and 20–100 W/m^2 for LH [Kalma et al., 2008; Kalma, 2008; Kustas and Norman, 2000].

[35] In Figure 9, the correlations coefficients (R^2) between reference and downscaled variables are presented for all the realizations and for all seasons. The values of R^2 are generally high, although there are notable differences across variables and seasons. The value of R^2 is more than 0.98 for TSK in all examined periods. For SMOIS and LH, the correlation is not as high but remains consistently above 0.8. The lowest R^2 values are observed in summer SMOIS (0.791) and winter LH (0.855), which is consistent with previous figures.

[36] Correct reproduction of the spatial continuity is the most important validation criterion for downscaling. To evaluate this, we compare the experimental variogram of

the reference downscaled variables with the experimental variograms from all 50 realizations. These are shown in Figure S5 (auxiliary material). The first feature to note is that the variograms of the downscaled models exhibit a good similarity with those of the reference. Another aspect of interest is that these variograms are unbounded (i.e., they do not stabilize at the variance value), meaning that the variables considered are nonstationary. This further reinforces and motivates the necessity of using specific techniques to address nonstationarity, as detailed in section 3.1.

4.3. Relationships Between Downscaled Variables

[37] The accuracy of the multivariate dependencies between variables is examined using scatter plots for both WRF reference variables and downscaled variables, with results presented in Figures 10 and 11 for the summer and winter seasons, respectively. The results for spring and autumn are shown in Figures S6 and S7, respectively (auxiliary material). The first row of each figure shows the downscaled variables, while the second row plots the WRF reference variables. In Figure 10, comparison of the scatter plots between downscaled and reference values demonstrate

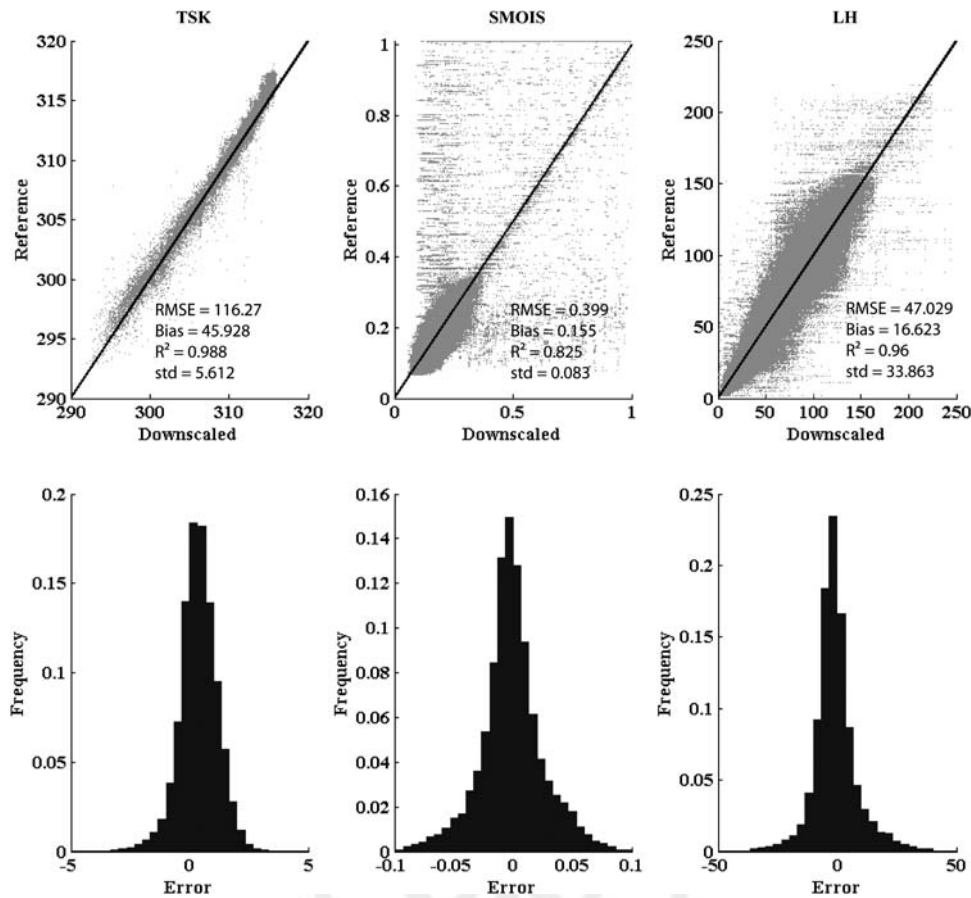


Figure 7. Scatter plots and errors in the downscaled TSK, SMOIS, and LH for the summer of 2006. Values for RMSE, correlation coefficient (R^2), and SD are shown.

that the three variables (TSK, SMOIS, and LH) present non-linear relationships with each other, due to the complex interactions between the land and atmosphere. The reproduction of the various nonlinear dependencies is excellent: a consequence of the multivariate capability of the DS method considering patterns between all of the variables. Note that there are known analytical relationships between the different variables LH, TSK, and SMOIS in the literature; however, our approach reproduces them not by physical modeling but by data driven, nonparametric sampling. The scatter plots vary over different seasons (see Figures 11, S6, and S7, auxiliary material) due to variation in the magnitudes of TSK, SMOIS, and LH. However, the reproduction of nonlinear dependencies remains excellent in all the cases.

5. Conclusion

[38] Downscaling of climate model data with the DS method was demonstrated through downscaling of WRF regional climate model outputs to reproduce seasonal values of temperature, SMOIS, and LH from 50 km resolution to a grid of 10 km over the MDB in southeast Australia. The DS algorithm samples patterns in a training image conditionally to different covariates that are available at a

coarser resolution. The training image is based on 20 years of data (1985–2005) at both coarse and fine scales. For each season, all of the variables are considered simultaneously in the training image. Given this rich inventory of spatial patterns, the DS approach is then used for downscaling for the following year 2006 but using only the coarse data. The nonstationarity in spatial features is considered in the simulation by providing the locational information in the training image. The spatial relationships among variables are not assumed to be the same over the different seasons, and the results show that these varying dependencies are correctly reproduced.

[39] The downscaled results from DS show excellent agreement with the spatial distribution of WRF reference variables at a fine scale for the TSK and LH across all seasons. The downscaled results for SMOIS show that DS is not able to reproduce some of the small-scale land surface features, especially over water bodies such as canals, lakes, and reservoirs. It is expected that this could be improved by using a land/water mask. The error analysis of the downscaled variables for all seasons and correlations among the variables show the potential of our approach in simultaneously producing statistical downscaling of multiple variables. The results are presented for one single

JHA ET AL.: A GEOSTATISTICAL APPROACH FOR DOWNSCALING

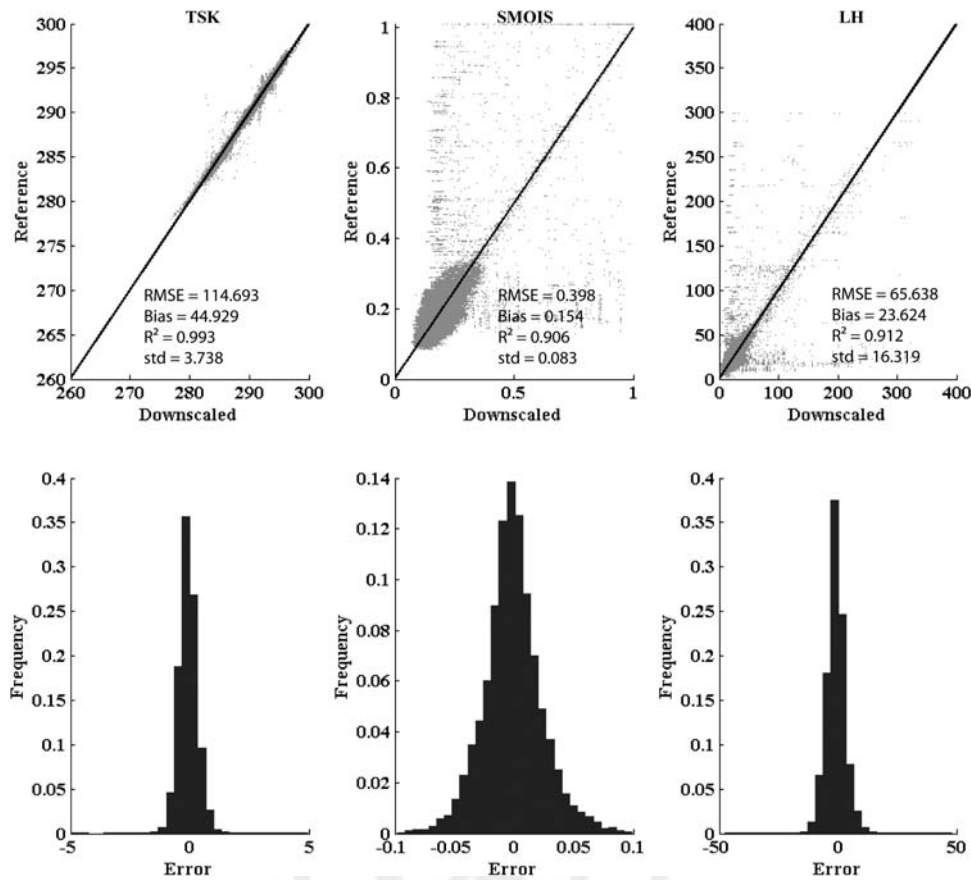


Figure 8. Scatter plots and errors in the downscaled TSK, SMOIS, and LH for the winter of 2006. Values for RMSE, correlation coefficient (R^2), and SD are shown.

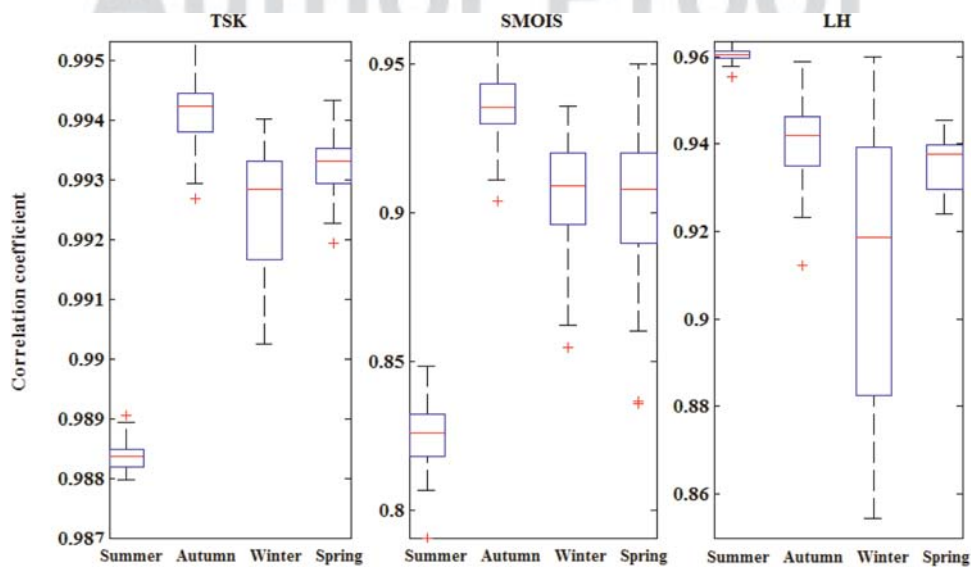


Figure 9. Correlation coefficient between downscaled and reference values for 50 realizations over summer, autumn, winter, and spring of 2006. Note the different ranges of correlation coefficients for each variable.

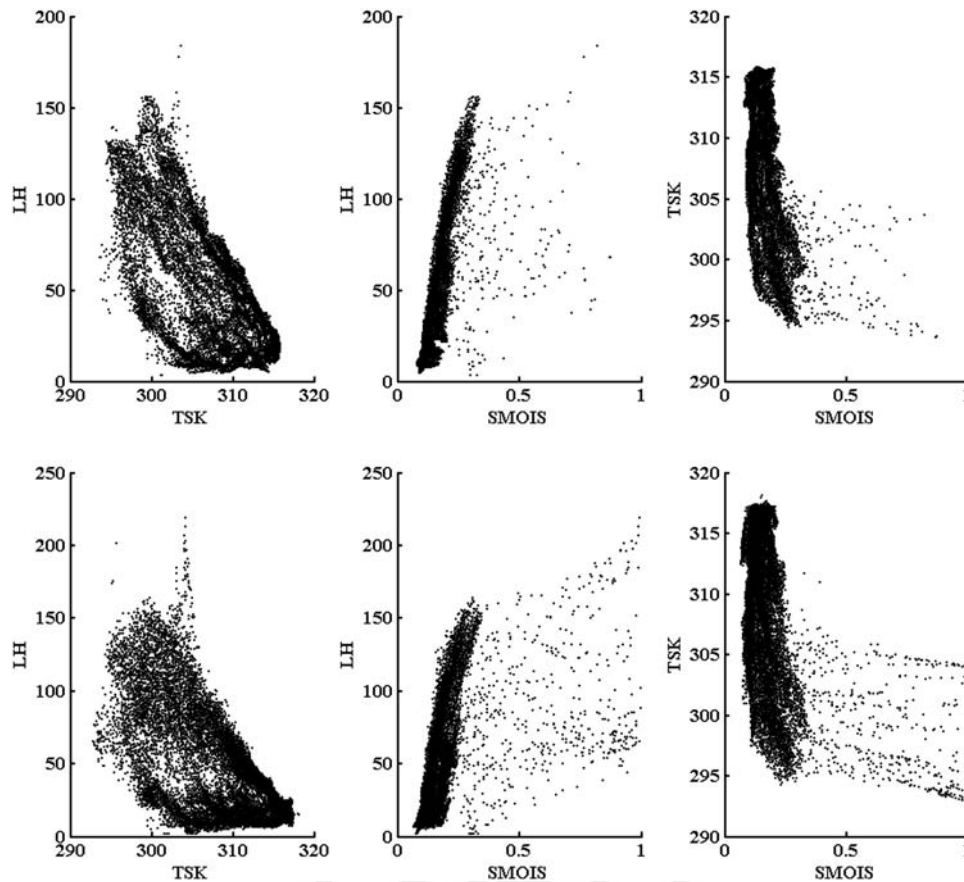


Figure 10. Characterizing the nonlinear relationship of downscaled and WRF reference variables for the summer of 2006. (top row) Scatter plots of values in the downscaled model. (bottom row) Scatter plots of values in the reference model.

realization of 50 possible realizations over which DS runs were performed. Acknowledging the fact that, all realizations are equiprobable, the multiple realizations are a representation of the uncertainty associated with the downscaling: a feature that other methods are generally unable to provide. Understanding the uncertainty in these reproductions is critical information for using the down-scaled forcing in applications such as rainfall-runoff models, groundwater models, or other operational systems designed to characterize hydrological and environmental response.

[40] Apart from providing an explicit capacity to represent uncertainty in the downscaled product, the DS approach also presents an advantage of reduced computational cost compared to RCMs. One full simulation of an RCM takes approximately 6000 CPU hours, while DS takes about 48 hours of CPU time for 50 realizations. The DS approach developed here also has a wide scope of application in the area of remote sensing and catchment studies, especially in feature sharpening or interpretation through image fusion [Agam *et al.*, 2007; Renzullo *et al.*, 2008], and gap filling in spatial data collected from satellites [Mariethoz *et al.*, 2012].

[41] One limitation of the approach is that training images must be available that contain both coarse and fine-scale variables. Building such training images requires that each coarse variable to be downscaled needs to be informed at the fine scale for some previous time steps. In our case, this information derives from model runs corresponding to previous time steps, but in practical applications, it could be beneficial to use remote sensing measurements. Such application with real-world remote sensing data is a focus of ongoing research. Another area of further research will examine the utility of this method for downscaling GCM outputs to local scales, based on observations at a daily time resolution. The methodology will be applied at the catchment scale, with the aim to downscale GCM outputs to fine-enough resolutions to meet the forcing data requirements of surface water-groundwater models. Such a study will enable an evaluation of the effects of climate change on groundwater resources. In evaluating future climate scenarios, it will be important to consider seasonal variability associated with extreme conditions responding to El Nino and La Nina occurrences. Examining the capacity of the DS approach to incorporate and reproduce such internal dynamics will allow a more robust representation of the observed system.

JHA ET AL.: A GEOSTATISTICAL APPROACH FOR DOWNSCALING

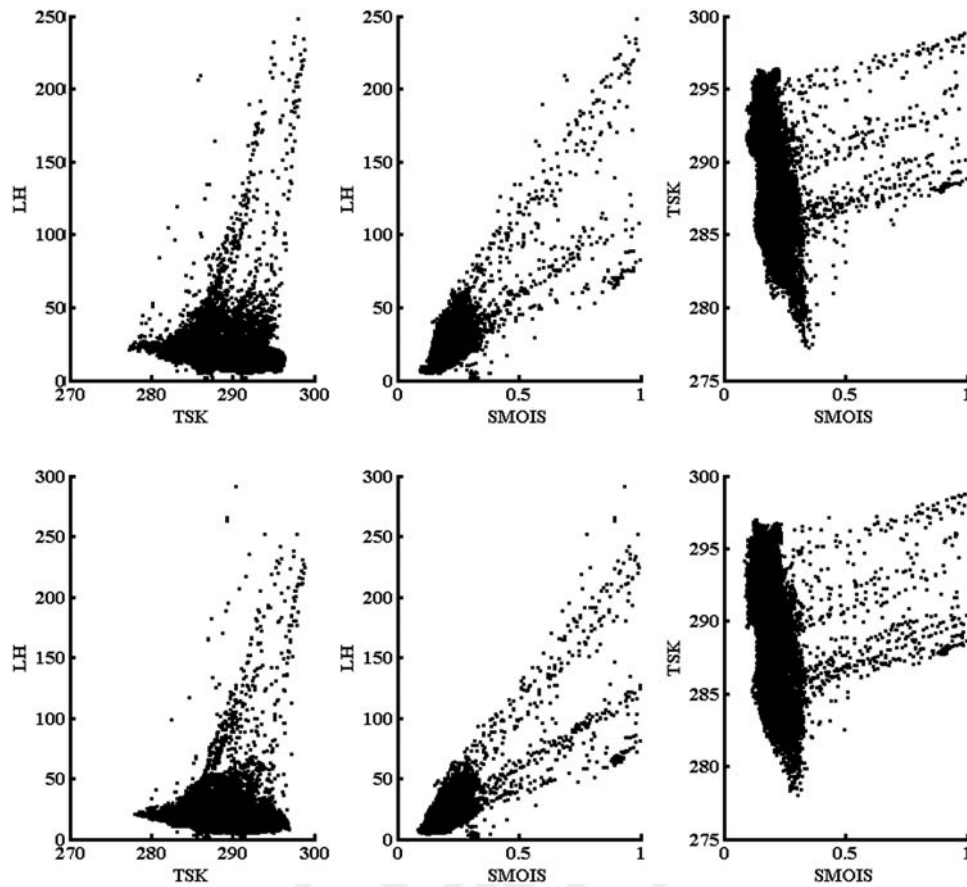


Figure 11. Characterizing the nonlinear relationship of downscaled and WRF reference variables for the winter of 2006. (Top row) Scatter plots of values in the downscaled model. (bottom row) Scatter plots of values in the reference model.

[42] **Acknowledgment.** This work was supported through a postdoctoral research fellowship as part of the National Centre for Groundwater Research and Training (NCGRT), a joint initiative between the Australian Research Council and the National Water Commission.

References

- Agam, N., W. P. Kustas, M. C. Anderson, F. Li, and C. M. U. Neale (2007), A vegetation index based technique for spatial sharpening of thermal imagery, *Remote Sens. Environ.*, 107(4), 545–558.
- Atkinson, P., E. Pardo-Igúzquiza, and M. Chica-Olmo (2008), Downscaling cokriging for super-resolution mapping of continua in remotely sensed images, *IEEE Trans. Geosci. Remote. Sens.*, 46(2), 573–580.
- Boucher, A. (2009), Sub-pixel mapping of coarse satellite remote sensing images with stochastic simulations from training images, *Math. Geosci.*, 41(3), 265–290.
- Brocca, L., T. Tullio, F. Melone, T. Moramarco, and R. Morbidelli (2012), Catchment scale soil moisture spatial-temporal variability, *J. Hydrol.*, 422–423, 63–75.
- Chu, J., J. Xia, C. Y. Xu, and V. Singh (2010), Statistical downscaling of daily mean temperature, pan evaporation and precipitation for climate change scenarios in Haihe River, China., *Theor. Appl. Climatol.*, 99(1), 149–161, doi:10.1007/s00704-009-0129-6.
- Drusch, M., E. F. Wood, H. Gao, and A. Thiele (2004), Soil moisture retrieval during the Southern Great Plains Hydrology Experiment 1999: A comparison between experimental remote sensing data and operational products, *Water Resour. Res.*, 40, W02504.
- Evans, J. P. (2012), Regional climate modelling: The future for climate change impacts and adaptation research, in *Articles, Climate Consensus, Earth Observation*, edited.
- Evans, J. P., and M. F. McCabe (2010), Regional climate simulation over Australia's Murray-Darling basin: A multitemporal assessment, *J. Geophys. Res. D: Atmospheres*, 115(14), D14114.
- Evans, J. P., and S. Westra (2012), Investigating the mechanisms of diurnal rainfall variability using a regional climate model, *J. Clim.*, 25, 7232–7247.
- Evans, J. P., A. J. Pitman, and F. T. Cruz (2011), Coupled atmospheric and land surface dynamics over southeast Australia: A review, analysis and identification of future research priorities, *Int. J. Climatol.*, 31, 1758–1772.
- Evans, J. P., J. L. McGregor, and K. McGuffie (2012), *Future Regional Climates. The Future of the World's Climate*, Elsevier, New York.
- Ferguson, C. R., and E. F. Wood (2010), An evaluation of satellite remote sensing data products for land surface hydrology: Atmospheric infrared sounder, *J. Hydrometeorol.*, 11, 1234–1262.
- Giorgi, F. (2006), Regional climate modeling: Status and perspectives, *J. Phys. IV France*, 139, 101–118.
- Gómez-Hernández, J. J., and X.-H. Wen (1998), To be or not to be multi-gaussian? A reflection on stochastic hydrogeology, *Adv. Water Resour.*, 21(1), 47–61.
- Goovaerts, P. (1997), *Geostatistics for Natural Resources Evaluation*, 496 pp., Oxford Univ. Press, Oxford.
- Hewitson, B. C., and R. Crane (1996), Climate downscaling: Techniques and application, *Clim. Res.*, 7(2), 85–95.
- Hoffmann, P., O. Krueger, and K. H. Schlunzen (2011), A statistical model for the urban heat island and its application to a climate change scenario, *Int. J. Climatol.*, 32, 1238–1248. doi:10.1002/joc.2348.
- Honarkhah, M., and J. Caers (2012), Direct pattern-based simulation of non-stationary geostatistical models, *Math. Geosci.*, 44(6), 651–672.
- Jiménez, C., et al. (2011), Global intercomparison of 12 land surface heat flux estimates, *J. Geophys Res. D*, 116(2), D02102, doi:10.1029/2010JD014545.

JHA ET AL.: A GEOSTATISTICAL APPROACH FOR DOWNSCALING

- Journal, A., and T. Zhang (2006), The necessity of a multiple-point prior model, *Math. Geol.*, 38(5), 591–610.
- Kalma, J. D., T. R. McVicar, and M. F. McCabe (2008), Estimating land surface evaporation: A review of methods using remotely sensed surface temperature data, *Surv. Geophys.*, 29(4), 421–469.
- Kidson, J. W., and C. S. Thompson (1998), A comparison of statistical and model based downscaling techniques for estimating local climate variations, *J. Clim.*, 11, 735–753.
- Kunstmann, H., K. Schneider, R. Forkel, and R. Knoche (2004), Impact analysis of climate change for an Alpine catchment using high resolution dynamic downscaling of ECHAM4 time slices, *Hydrol Earth Syst Sci.*, 8(6), 1030–1044.
- Kustas, W. P., and J. M. Norman (2000), Evaluating the effects of subpixel heterogeneity on pixel average fluxes, *Remote Sens. Environ.*, 74, 327–342.
- Kyriakidis, P. C. (2004), A geostatistical framework for area-to-point spatial interpolation, *Geogr. Anal.*, 36(3), 259–289.
- Kyriakidis, P. C., and E.-H. Yoo (2005), Geostatistical prediction and simulation of point values from areal data, *Geogr. Anal.*, 37(2), 124–151.
- Liu, L., P. J. Li, and D. F. Ma (2007), Remote sensing image fusion based on cokriging methods, *Remote Sens. Land Resour.*, 73, 8–12.
- Liu, L., Z. Liu, X. Ren, T. Fischer, and Y. Xu (2011), Hydrological impacts of climate change in the Yellow River Basin for the 21st century using hydrological model and statistical downscaling model, *Quat Int.*, 244(2), 211–220.
- Liu, Y. Y., J. P. Evans, M. F. McCabe, R. A. M. de Jeu, A. I. J. M. van Dijk, and H. Su (2010), Influence of cracking clays on satellite estimated and model simulated soil moisture, *Hydrol Earth Syst Sci.*, 14, 979–990, doi:10.5194/hess-14-979-2010.
- Manfreda, S., M. F. McCabe, M. Fiorentino, I. Rodriguez-Iturbe, and E. F. Wood (2007), Scaling characteristics of spatial patterns of soil moisture from distributed modelling, *Adv. Water Resour.*, 30(10), 2145–2150.
- Maraun, D., et al. (2010), Precipitation downscaling under climate change: Recent developments to bridge the gap between dynamical models and the end user, *Rev. Geophys.*, 48(3), RG3003.
- Mariethoz, G., and B. F. J. Kelly (2011), Modeling complex geological structures with elementary training images and transform-invariant distances, *Water Resour. Res.*, 47(7), W07527, doi:10.1029/2011WR010412.
- Mariethoz, G., P. Renard, and J. Straubhaar (2010), The direct sampling method to perform multiple-point geostatistical simulations, *Water Resour. Res.*, 46(11), W11536, doi:10.1029/2008WR007621.
- Mariethoz, G., P. Renard, and J. Straubhaar (2011), Extrapolating the fractal characteristics of an image using scale-invariant multiple-point statistics, *Math. Geosci.*, 43(7), 783–797.
- Mariethoz, G., M. F. McCabe, and P. Renard, (2012), Spatiotemporal reconstruction of gaps in multivariate fields using the direct sampling approach, *Water Resour. Res.*, 48, W10507, doi:10.1029/2012WR012115.
- McCabe, M. F., H. Gao, and E. F. Wood (2005a), Evaluation of AMSR-E derived soil moisture retrievals using ground-based and PSR airborne data during SMEX02, *J. Hydrometeorol.*, 6, 864–877.
- McCabe, M. F., E. F. Wood, and H. Gao (2005b), Initial soil moisture retrievals from AMSR-E: Multiscale comparison using in situ data and rainfall patterns over Iowa, *Geophys. Res. Lett.*, 32, L06403, doi:10.1029/2004GL021222.
- McCabe, M. F., E. F. Wood, R. Wojcik, M. Pan, J. Sheffield, H. Gao, and H. Su (2008a), Hydrological consistency using multi-sensor remote sensing data for water and energy cycle studies, *Remote Sens. Environ.*, 112(2), 430–444.
- McCabe, M. F., L. K. Balick, J. Theiler, A. R. Gillespie, and A. Mushkin (2008b), Linear mixing in thermal infrared temperature retrieval, *Int. J. Remote Sens.*, 29, 5047–5061.
- McCumber, M., and R. Pielke (1981), Simulation of the effects of surface fluxes of heat and moisture in a mesoscale numerical model. 1. Soil layer, *J. Geophys. Res.*, 86(C10), 9929–9938. doi:10.1029/JGREA000086000 C10009929000001.
- Meerschman, E., G. Piro, G. Mariethoz, J. Straubhaar, M. Van Merivenne, and P. Renard (2012), A practical guide to performing multiple-point geostatistical simulations with the direct sampling algorithm, *Comput. Geosci.*, in press.
- Nishii, R., S. Kusanobu, and S. Tanaka (1996), Enhancement of low spatial resolution image based on high resolution-bands., *IEEE Trans. Geosci. Remote Sens.*, 34, 1151–1158.
- Pardo-Iguzquiza, E., M. Chica-Olmo, and P. M. Atkinson (2006), Downscaling cokriging for image sharpening, *Remote Sens. Environ.*, 102, 86–98.
- Pardo-Iguzquiza, E., P. M. Atkinson, and M. Chica-Olmo (2010), DSCOKRI: A library of computer programs for downscaling cokriging in support of remote sensing applications, *Comput. Geosci.*, 36(7), 881–894, 810, doi:10.1016/j.cageo.2009.10.1006.
- Raje, D., and P. P. Mujumdar (2011), A comparison of three methods for downscaling daily precipitation in the Punjab region, *Hydrol. Processes*, 25, 3575–3589.
- Renzullo, L. J., D. J. Barrett, A. S. Marks, M. J. Hill, J. P. Guerschman, and Q. Mu (2008), Multi-sensor model-data fusion for estimation of hydrologic and energy flux parameters, *Remote Sens. Environ.*, 112, 1306–1319.
- Rodriguez-Iturbe, I. (2000), Ecohydrology: A hydrologic perspective of climate-soil-vegetation dynamics, *Water Resour. Res.*, 36(1), 3–9.
- Sain, S. R., R. Furrer, and N. Cressie (2011), A spatial analysis of multivariate output from regional climate models, *Ann. Appl. Stat.*, 5(1), 150–175.
- Segui, P. Q., A. Ribes, E. Martin, F. Habets, and J. Boe (2010), Comparison of three downscaling methods in simulating the impact of climate change on the hydrology of Mediterranean basins, *J. Hydrol.*, 383, 111–124.
- Shannon, C. (1948), A mathematical theory of communication, *Bell Syst. Tech. J.*, 27, 379–423.
- Stoll, S., H. J. H. Franssen, M. Butts, and W. Kinzelbach (2011), Analysis of the impact of climate change on groundwater related hydrological fluxes: A multi-model approach including different downscaling methods, *Hydrol Earth Syst. Sci.*, 15, 21–38.
- Strebelle, S. (2002), Conditional simulation of complex geological structures using multiple-point statistics, *Math. Geol.*, 24(1), 1–22.
- Teutschbein, C., F. Wetterhall, and J. Seibert (2011), Evaluation of different downscaling techniques for hydrological climate-change impact studies at the catchment scale, *Clim. Dyn.*, 37, 2087–2105. doi:10.1007/s00382-010-0979-8.
- Walker, J., and P. R. Rowntree (1977), The effect of soil moisture on circulation and rainfall in a tropical model, *Q. J. R. Meteorol. Soc.*, 103, 29–46.
- Wallace, J. M., and P. V. Hobbs (2006), *Atmospheric Science: An Introduction Survey*, Elsevier, Oxford.
- Wan, Z., Y. Zhang, Q. Zhang, and Z.-L. Li (2002), Validation of the land-surface temperature products retrieved from terra moderate resolution imaging spectroradiometer data, *Remote Sens. Environ.*, 83, 163–180.
- Wilby, R., and T. Wigley (1997), Downscaling general circulation model output: A review, *Prog. Phys. Geogr.*, 21(4), 530–548.
- Wilby, R., Dawson, C. W., and Barrow, E. M. (2002), SDSM—A decision support tool for the assessment of regional climate change impacts, *Environ. Modell. Softw.*, 17(2), 145–157.
- Zhang, X., H. Jiang, G. Zhou, Z. Xiao, and Z. Zhang (2012), Geostatistical interpolation of missing data and downscaling of spatial resolution for remotely sensed atmospheric methane column concentrations, *Int. J. Remote Sens.*, 33(1), 120–134.

Author Queries

AQ1: Please check whether the edit made to the title is appropriate.

AQ2: Please provide the details such as the paper title, journal title, and year of submission for the reference citation “Meerschman et al. [submitted].”

AQ3: Please provide the editors and publisher and its location details for the reference “Evans, J. P. (2012a).”

AQ4: Please note as there are two McCabe et al. [2008] “a” and “b” are added to differentiate them and their citations.

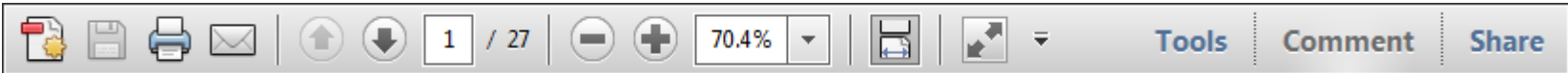
AQ5: Please update “Meerschman et al. [2012]” if possible.



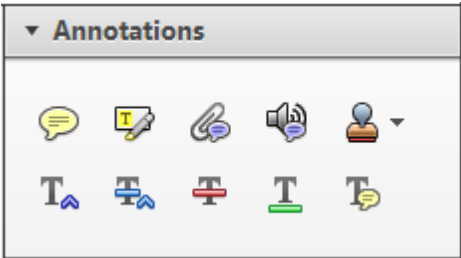
Author Proof

Required software to e-Annotate PDFs: Adobe Acrobat Professional or Adobe Reader (version 8.0 or above). (Note that this document uses screenshots from Adobe Reader X)
The latest version of Acrobat Reader can be downloaded for free at: <http://get.adobe.com/reader/>


Once you have Acrobat Reader open on your computer, click on the [Comment](#) tab at the right of the toolbar:



This will open up a panel down the right side of the document. The majority of tools you will use for annotating your proof will be in the [Annotations](#) section, pictured opposite. We've picked out some of these tools below:



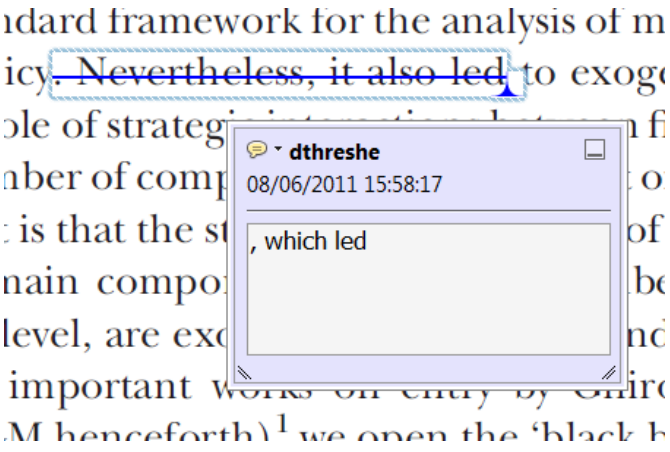
1. [Replace \(Ins\)](#) Tool – for replacing text.




Strikes a line through text and opens up a text box where replacement text can be entered.

How to use it

- Highlight a word or sentence.
- Click on the [Replace \(Ins\)](#) icon in the Annotations section.
- Type the replacement text into the blue box that appears.



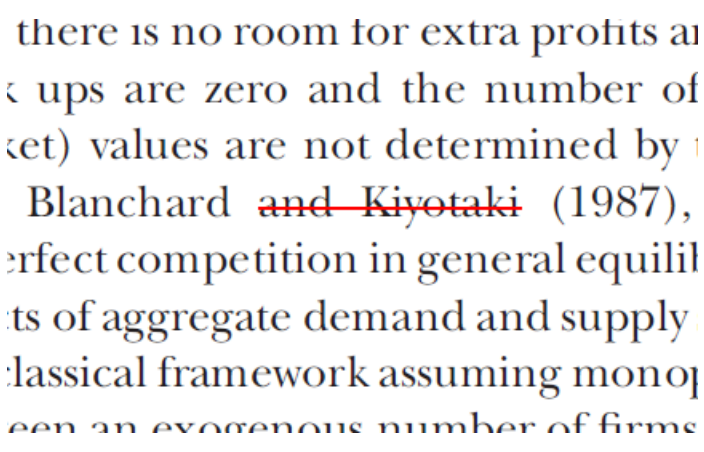
2. [Strikethrough \(Del\)](#) Tool – for deleting text.




Strikes a red line through text that is to be deleted.

How to use it

- Highlight a word or sentence.
- Click on the [Strikethrough \(Del\)](#) icon in the Annotations section.



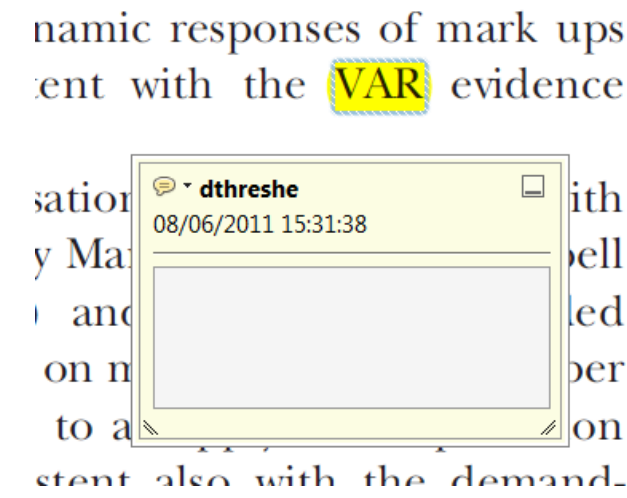
3. [Add note to text](#) Tool – for highlighting a section to be changed to bold or italic.



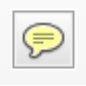
Highlights text in yellow and opens up a text box where comments can be entered.

How to use it

- Highlight the relevant section of text.
- Click on the [Add note to text](#) icon in the Annotations section.
- Type instruction on what should be changed regarding the text into the yellow box that appears.



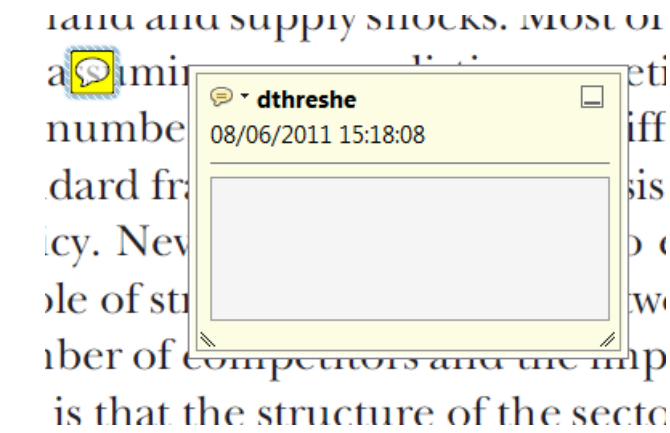
4. [Add sticky note](#) Tool – for making notes at specific points in the text.




Marks a point in the proof where a comment needs to be highlighted.

How to use it

- Click on the [Add sticky note](#) icon in the Annotations section.
- Click at the point in the proof where the comment should be inserted.
- Type the comment into the yellow box that appears.



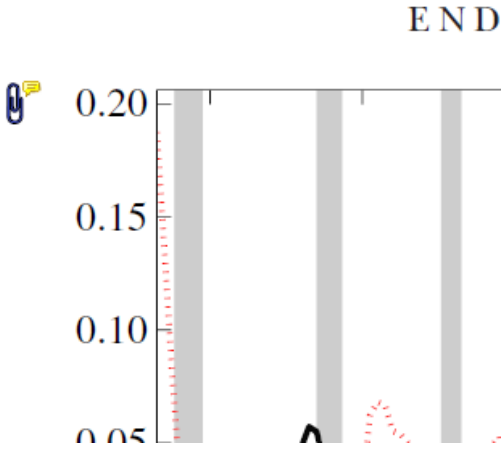
5. **Attach File** Tool – for inserting large amounts of text or replacement figures.




Inserts an icon linking to the attached file in the appropriate place in the text.

How to use it

- Click on the **Attach File** icon in the Annotations section.
- Click on the proof to where you'd like the attached file to be linked.
- Select the file to be attached from your computer or network.
- Select the colour and type of icon that will appear in the proof. Click OK.



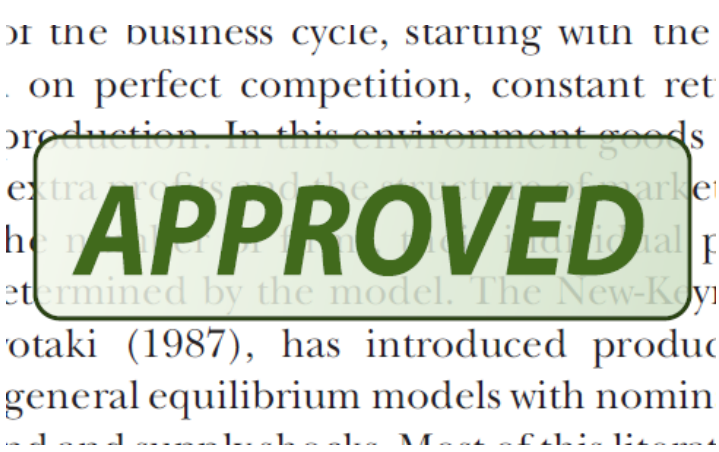
6. **Add stamp** Tool – for approving a proof if no corrections are required.




Inserts a selected stamp onto an appropriate place in the proof.

How to use it

- Click on the **Add stamp** icon in the Annotations section.
- Select the stamp you want to use. (The **Approved** stamp is usually available directly in the menu that appears).
- Click on the proof where you'd like the stamp to appear. (Where a proof is to be approved as it is, this would normally be on the first page).



Drawing Markups

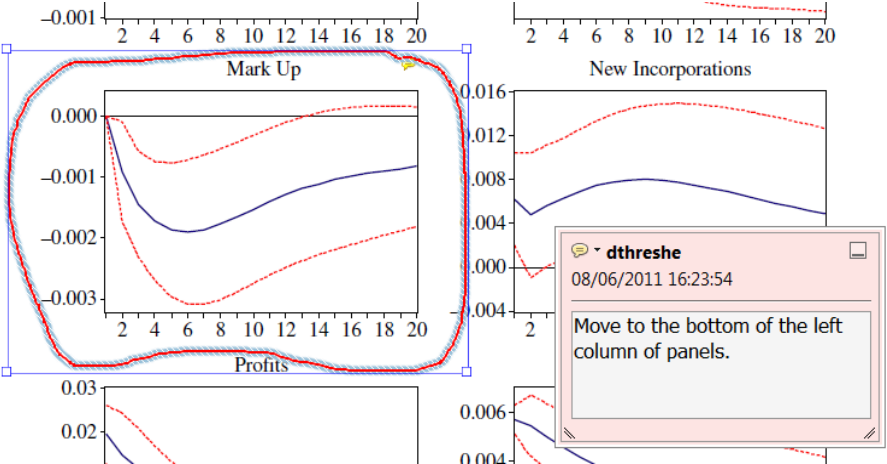


How to use it

- Click on one of the shapes in the **Drawing Markups** section.
- Click on the proof at the relevant point and draw the selected shape with the cursor.
- To add a comment to the drawn shape, move the cursor over the shape until an arrowhead appears.
- Double click on the shape and type any text in the red box that appears.

7. **Drawing Markups** Tools – for drawing shapes, lines and freeform annotations on proofs and commenting on these marks.

Allows shapes, lines and freeform annotations to be drawn on proofs and for comment to be made on these marks..



For further information on how to annotate proofs, click on the **Help** menu to reveal a list of further options:

Article Page Charge Form

Instructions:

1. Enter the Article Number as it appears on your article.
2. Enter the final number of Pages in Article as it appears in your proof.
3. Select the Journal Name from the dropdown list; this will determine the Publication Fee and the Excess Length Fee (if applicable).
4. Check and confirm your selections, as they will generate your Total Cost.
 - a. Publication Fee refers to the flat fee for article publication per journal.
 - b. Excess Length Fee (\$250 per page) applies to pages >13 for all journals, except *Geophysical Research Letters*, for which it applies to pages >5.
5. Check the box for OnlineOpen (which will negate your page fees) if you'd like for your article to be open access and fill out the form on this page:
https://authorservices.wiley.com/bauthor/onlineopen_order.asp.
6. Authorize Wiley to process a final invoice upon publication in an issue via the Signature line.
7. Enter the billing name and address. The Wiley Reprints Department will use the information provided to invoice charges.
8. Click "Submit" to e-mail this form as an attachment to the Production Editor. If your local mail client does not launch, please save this form and send it as an attachment to _____.

Article Number		Fill in all billing contact information below to accept the Total Cost on the left.
Pages in Article		
Journal Name		
Publication Fee	\$	
Excess Length Fee per Page	\$	
OnlineOpen?		
Total Cost: \$ _____		
Signature: _____		Name:
		Address:
		Phone:
		E-mail:



Additional reprint and journal issue purchases

Should you wish to purchase additional copies of your article, please click on the link and follow the instructions provided:
<https://caesar.sheridan.com/reprints/redir.php?pub=10089&acro=WRCR>

Corresponding authors are invited to inform their co-authors of the reprint options available.

Please note that regardless of the form in which they are acquired, reprints should not be resold, nor further disseminated in electronic form, nor deployed in part or in whole in any marketing, promotional or educational contexts without authorization from Wiley. Permissions requests should be directed to mailto: permissionsus@wiley.com

For information about 'Pay-Per-View and Article Select' click on the following link: <http://wileyonlinelibrary.com/ppv>